Indicator of Flood-Irrigated Crops From SMOS and SMAP Soil Moisture Products in Southern India

Claire Pascal, Sylvain Ferrant, Nemesio Rodriguez-Fernandez, Yann Kerr, Adrien Selles, Olivier Merlin

Indicator of flood-irrigated crops from SMOS and SMAP soil moisture products in southern India

Claire Pascal[1], Sylvain Ferrant[1], Nemesio Rodriguez-Fernandez[1], Yann Kerr[1], Adrien Selles[2], Olivier Merlin[1]
[1]Centre d'Étude Spatiale de la BIOsphère (CESBIO-UPS-CNRS-IRD-CNES-INRAE), 18 av. Ed. Belin, Toulouse CEDEX 9, 31401, France
[2]Bureau de Recherches Géologiques et Minières (BRGM), Université de Montpellier, 1039 rue de Pinville, Montpellier, 34000, France

***Abstract*—Spaceborne L-band data have the potential to monitor flooded and irrigated areas. However, further studies are needed to assess in real cases the impact of flood-irrigated crops on SMOS and SMAP surface soil moisture (SSM) data. This paper demonstrates the ability of SMOS/SMAP SSM retrievals to quantify the fraction of flood-irrigated area at the seasonal scale and at a 25 km resolution in the Telangana State in southern India. Over irrigated areas, both SMOS level 3 (L3) SSM and SMAP L3 enhanced SSM products present a bimodal annual cycle, with a peak of SSM during the monsoon (wet) season corresponding to rainfall and irrigation, and a peak during the dry season due to irrigation activities solely. The second peak is absent or has a very small amplitude in areas where rice represents a small fraction (typically below 5-10%). More importantly, the amplitude of the second SSM peak is significantly correlated to the rice cover fraction within 25$\times$25 km^2 pixels (R=0.81 for SMOS and 0.77 for SMAP), showing its potential to assess crop fraction and hence the water used for irrigation. The SMOS/SMAP L3 SSM peak during the dry period occurs several months before the harvest, constituting an indicator for rice stocks at the end of the season. However the irrigation signature is absent from the SMAP level 4 SSM product derived from the assimilation of SMAP brightness temperatures in a land surface model, which indicates that the data assimilation scheme is inefficient to restitute irrigation information.**

***Index Terms*—Soil moisture, SMOS, SMAP, Irrigation, Water Management, Rice Cropping, Regional Scale.**

I. Introduction

With the increase of agricultural production during the last century, irrigation has become the first consumer of freshwater, representing 70% of global freshwater withdrawals [1]. The increase of soil moisture by irrigation practices also alters the water cycle [2]. Knowledge of irrigated land is hence crucial to manage the water resource and to ensure food security. It is also important to understand the impact of irrigation on the water cycle and climatology, and to participate to the development of hydrological models that account for irrigation in a realistic manner.

The dynamic mapping of inundated areas can be achieved with microwave radiometers thanks to the high sensitivity of the microwave brightness temperature (Tb) to open water. Such data are insensitive to clouds and hence allow continuous monitoring, in spite of having a lower spatial resolution than optical data. The Tb at various frequencies has been used to detect flooded pixels [3]–[6] or to estimate an open water fraction within the microwave pixel by separating the contributions of land and water. Especially, Tb data from the multi-band Advanced Microwave Scanning Radiometer for EOS (AMSR-E) sensor [7], [8], the L-band Soil Moisture and Ocean Salinity (SMOS) mission [9], and the L-band Soil Moisture Active Passive (SMAP) mission [5] have been used at the 5 km and $\simeq$40 km resolution for AMSR-E (89 GHz) and SMOS/SMAP, respectively. Note that higher resolutions can be achieved by downscaling the microwave data using disaggregation algorithms and ancillary data [5], [10].

The particular sensitivity of the L-band (1.4 GHz) to water has been used to monitor the soil water content. Since 2010 and 2015 respectively, SMOS and SMAP satellite missions have provided surface soil moisture (SSM) estimates every 3 days at a $\simeq$40 km resolution. L-band-derived SSM data have been proven to be sensitive to irrigation, in particular in heavily and flood irrigated areas [11], [12], demonstrating their potential for irrigated area mapping and irrigation timing detection. Notably, several indicators have been identified to detect irrigation from the amplitude of SSM values in time series [11] and using the spatial relative difference within an area revealing the spatial distribution of irrigated sites [13]. Also, irrigated areas can be detected by comparing the SSM retrievals with the SSM simulated by a land surface model that does not take irrigation into account: larger observed SSM values are attributed to irrigation [12]–[14]. Automatic discrimination of irrigated areas from other land types has also been achieved from SSM data with unsupervised classification algorithms [13].

As a step further, L-band-derived SSM data have also been used to estimate the quantity of water used for irrigation [15]–[18]. Especially, the SM2RAIN algorithm [19] is based on the inversion of the soil water balance equation. This requires prior calibration during rainy periods, by assuming that there is no irrigation during those periods. Such an approach has been effective in quantifying irrigation water use over large irrigated areas and where irrigation and precipitation periods are distinct. However, SM2RAIN is not able to separate the contributions of rainfall and irrigation to the observed SSM dynamics [15]. Moreover, its application to smaller and sparse irrigated areas would require disaggregated SSM data, which may not be available at the required spatio-temporal scales with a sufficient accuracy [20].

To this day, therefore, studies have mainly focused on the binary discrimination of irrigated and non-irrigated pixels from

the SSM signals. However the microwave pixels (several tens of km) are generally much larger than the size of agricultural fields or even often the size of irrigation districts, and hence the above methods do not provide sub-pixel information about the portion of irrigated areas. In particular, further studies are needed to assess the ability of L-band-derived SSM to estimate the fraction of irrigated areas within SMOS and SMAP pixels, in the same way that the open fraction water can be estimated from Tb data. In this context, this paper aims to quantify the sensitivity of SMOS and SMAP SSM data to the percentage of irrigated rice within 25 km resolution (SMOS sampling grid) pixels. The study is undertaken over the Telangana State in southern India and for four years when field data are available (2016 to 2019 included). The reference data of rice fraction at the 25 km resolution are derived from an existing supervised classification algorithm [21], [22] based on Sentinel-2 data and previously evaluated using ground measurements in the area.

II. Study area and data

A. Study area

The study focuses on the Telangana State in southern India (see Figure 1). Highly rural and irrigated (15% of the State area [23]), Telangana is dominated by a monsoon climate alternating with a wet and dry season. Monsoon rainfall occurs between July and October and ranges between 540 and 1300 mm a year with an average of 879 mm (Indian Meteorological Department, https://mausam.imd.gov.in/). Annual precipitation sustains generally two growing seasons of irrigated crops in a year, one during the wet season (from July to November) and one during the dry season (from January to April). Orchards, vegetables and maize are irrigated, but rice is by far the largest consumer of irrigation water in the area [24]. Rice is flooded from early July until early September and from early January until early March in the wet and dry season respectively.

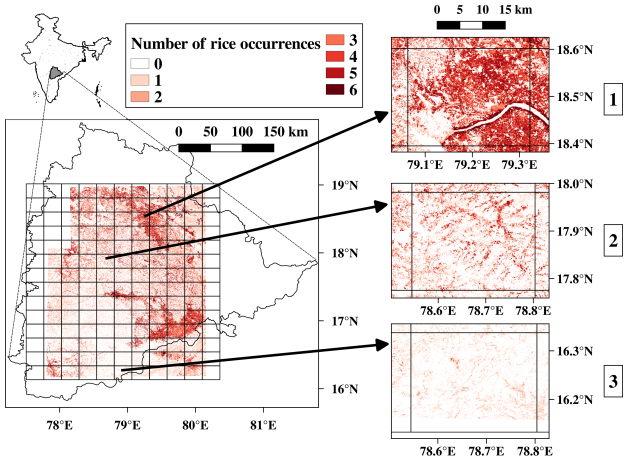

Fig. 1. Overview of the study area within the Telangana state in India overlaid with the 25 km resolution SMOS sampling grid and the number of rice occurrences during the 6 seasons when land cover maps are available.

B. Data

This section presents the reference rice cover maps, SMOS/SMAP SSM data and other ancillary (vegetation index and rainfall) data used to interpret the results. All data were resampled (by simple averaging) on the same 25 km resolution SMOS grid.

1) Land cover maps: Reference land cover maps were produced from Sentinel-2 reflectances for wet and dry seasons from 2016 to 2019 separately on 8 Sentinel-2 tiles of 100×100 km^2 each at 10 m resolution. Sentinel-2 data were processed by the MAJA processing chain [25] which detects clouds, cloud and topographic shadows, and corrects reflectance levels for atmospheric phenomena (absorption by atmospheric gases and scattering by air molecules and aerosols). These images were downloaded from Theia data platform (https://www.theia-land.fr/). Rice cover maps are produced with the IOTA2 algorithm (Infrastructure pour l'Occupation des sols par Traitement Automatique Incorporant les Orfeo Toolbox Applications, https://framagit.org/iota2-project/iota2), that achieves a supervised multitemporal classification with a random forest algorithm on the time series of Sentinel-2 images interpolated at 10 days [22]. The land cover classifications in wet and dry seasons are made on images acquired between July and November and between January and April, respectively.

The samples used for learning and evaluation of the classification algorithm are field data acquired on several consecutive days during each season of each year. Field data consist in visual identification of homogenous land cover and their delimitation as polygons using a GPS to locate them [21]. The performance of the rice cropping classification is evaluated with the F-score. The F-score is the harmonic mean of (i) the recall, i.e. the ability of the algorithm to identify a rice pixel, and (ii) the precision that measures the purity of the rice class. The rice class is generally deemed reliable with a F-score ranging from 75% to 92%. The interannual variability of the performances is linked to (i) the number of samples that varies between the years (262 to 1669) and (ii) the number of available Sentinel-2 images, which can significantly change during the wet season due to cloud coverage. In particular, the maps produced for the wet seasons of 2016 and 2017 are not used in this study because of their poor performance (F-score below 20%). Figure 1 shows the number of rice occurrences at the 10 m resolution during the 6 seasons when land cover maps are available.

The seasonal rice cover fraction is then estimated within each 25 km resolution SMOS grid pixel by averaging all 10 m pixels.

2) SMOS: The SMOS mission was launched in November 2009 and has a revisit time of 3 days at the Equator. The SMOS satellite carries an interferometric radiometer working at L-band. The data used for this study are the monthly level 3 (L3) SSM (L3SM RE07) in the first 5 centimeters of soil, provided by the Centre Aval de Traitement des Données SMOS (CATDS, https://www.catds.fr/) [26]. The data have a $\simeq$40 km resolution on average but are distributed on the 25 km resolution EASE2 grid [27] for both ascending and descending orbits. In this study we use the monthly average SSM of both orbits.

3) SMAP: The SMAP satellite, launched in January 2015, carries an L-band passive microwave radiometer. It provides SSM estimates at $\simeq$40 km resolution with a revisit time of

3 days at the Equator. The data used for this study are the enhanced L3 dataset (L3E) provided on a 9 km resolution grid and obtained by exploiting the oversampling of the antenna overpasses. In this study we use the average SSM of both orbits. We also use the SMAP level 4 (L4) SSM data which are obtained by assimilating the SMAP Tb in the NASA Catchment Land surface Model (CLM) using an ensemble Kalman filter [28]. The model describes the vertical transfer of soil moisture between the surface and root zone reservoirs, and provides fields of SSM and root zone soil moisture globally at 9 km resolution every 3 hours. The model is driven with observation-based surface meteorological forcing data, including precipitation, but does not account for irrigation activities. We use both L3 and L4 SSM data aggregated at the monthly scale and averaged within the 25 km pixels of the SMOS grid.

4) MODIS NDVI: The monthly NDVI (Normalized Difference Vegetation Index) allows monitoring the state of vegetation at a temporal scale finer than that of the seasonal land cover maps. We use the monthly NDVI of MODIS (Moderate-Resolution Imaging Spectroradiometer) sensor aboard Terra and Aqua satellites (launched in 1999 and 2002, respectively), at 1 km resolution (MOD13A3v006) and averaged within the 25 km pixels of the SMOS grid.

5) GPM IMERG rainfall: The Integrated Multi-satellitE Retrievals algorithm provides a rainfall product that combines information from the Global Precipitation Measurement mission (2014-present). We use monthly rainfall rates, provided at a resolution of 0.1° and resampled (bilinear resampling) on the 25 km resolution SMOS grid.

III. Results and Discussion

A. SSM dynamics over contrasted areas

The sensitivity of L-band sensors to irrigation is illustrated by the comparison of SMOS/SMAP SSM time series on three contrasted 25×25 km^2 pixels, numbered from 1 to 3 (see Figure 1): 1) a heavily irrigated one (from 10 to 60% of rice cover) supplied with water by the irrigation systems downstream of large dams, 2) an upstream irrigated area where rice sowing is limited by the lack of water availability, and 3) a pixel with a dominant forest cover. Figure 2 shows the time series of 25 km resolution SMOS L3, SMAP L3E and SMAP L4 SSM monthly anomalies (obtained by subtracting the temporal average of SSM values between 2016 and 2019 pixel-wise) averaged within each 25×25 km^2 pixel. The percentage of rice cover is shown for wet (large bands) and dry (thin hatched bands) seasons. The monthly NDVI indicates the crop/vegetation growth at higher temporal resolution.

In heavily irrigated areas (as in pixel 1), the SSM retrieved from SMOS and SMAP sensors has a bimodal annual cycle. During the wet season, the first peak of SSM is correlated with the precipitation, and the contribution of irrigation to SSM cannot be easily disentangled. During the dry season, SMOS and SMAP SSM show a systematic augmentation in the dry season, between December and March. The maximum SSM value of the second peak is reached generally in January or February, when rice crops are flooded. The absence of precipitation coinciding with this peak suggests an anthropogenic source. The peak of NDVI two months later, associated with crop growth, strengthens this interpretation.

In upstream irrigated areas (as in pixel 2), the rice cover is lower and rarely exceeds 20% because of the lack of water availability, particularly during the dry season. SSM still has a bimodal cycle, but with lower amplitude for the SSM peaks in the dry season (SSM anomaly of 0.05 m^3/m^3 at most), while the NDVI presents a single annual peak.

By contrast, the SSM of non-irrigated areas (as in pixel 3) presents a single peak in the year during the wet season which has its origins in monsoon rainfall. The different behaviors of SSM dynamics over irrigated and not irrigated areas confirm the findings of [11] in the western United States.

Contrary to SMOS and SMAP L3 SSM, SMAP L4 SSM does not show a peak in the dry season in irrigated areas and seems correlated solely to rainfall. This corroborates the limitations of assimilation approaches in representing unmodeled processes [14]. Two reasons can explain this result: first, an incorrect forcing of the model that integrates the contribution of rainfall but not irrigation to soil moisture, and second, the high dependency of assimilation results to the weights and uncertainties associated with observations and models.

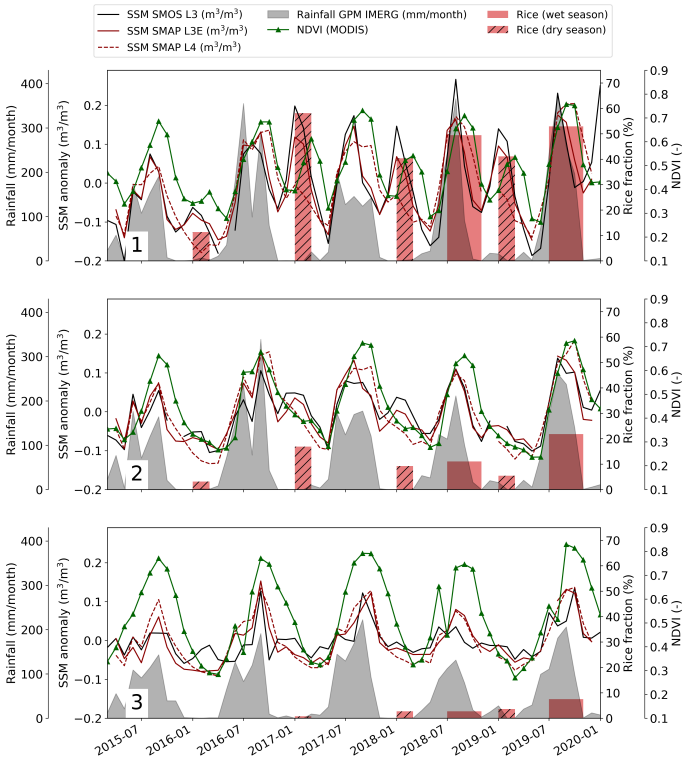

Fig. 2. Time series of monthly anomalies of SMOS and SMAP SSM (obtained by subtracting the temporal average of SSM values between 2016 and 2019 pixel-wise), GPM IMERG rainfall, MODIS NDVI, and seasonal land cover fraction (%) on three pixels of 25×25 km^2. First axis: GPM IMERG rainfall (mm/month). Second axis: SMOS L3 (black line), SMAP L3E (solid dark red line) and SMAP L4 (dotted dark red line) SSM. Third axis: Land cover fraction (%) for wet (large bands) and dry (thin hatched bands) season. Fourth axis: MODIS NDVI (solid green line).

TABLE I
PEARSON CORRELATION COEFFICIENTS BETWEEN RICE COVER (%) AND SSM FOR EVERY SEASON OF EACH YEAR OR FOR ALL YEARS ("ALL"). ALL SIGNIFICANT CORRELATIONS ARE ASSOCIATED WITH A P-VALUE BELOW 0.05.

Season	Year	SMOS L3		SMAP L3E		SMAP L4	
		R	p-value	R	p-value	R	p-value
Dry	2016	0.67	3.7e-19	0.58	1.7e-13	*0.05*	*0.6*
	2017	0.89	8.6e-47	0.77	2.4e-26	0.55	3.9e-12
	2018	0.86	1.5e-41	0.67	6.5e-18	0.36	1.5e-05
	2019	0.62	1.2e-15	0.71	3.8e-22	0.56	1.0e-12
	All	0.81	1.3e-107	0.77	1.6e-96	0.55	8.1e-18
Wet	2018	0.76	4.8e-27	0.63	2.1e-16	0.44	6.9e-08
	2019	0.65	9.5e-18	0.56	1.1e-12	0.24	4.2e-3
	All	0.68	4.8e-38	0.55	7.1e-23	0.34	1.0e-08

B. *Spatio-temporal analysis*

At the scale of each 25 km resolution pixel, the amplitude of the SSM peak is generally correlated in time with the corresponding proportion of rice cultivated within the area. This is illustrated in Figure 2 on pixel 1, in which a small proportion of rice is sown during the 2016 dry season (11% of rice) due to a lack of available water after a succession of dry years. This situation explains a low SSM peak amplitude (SSM anomaly of -0.05 m^3/m^3). On the other hand, the heavy monsoon rainfall in September 2016 has replenished surface and groundwater that allowed a large rice cultivation in the following 2017 dry season (58% of rice for a SSM anomaly of 0.1 and 0.2 m^3/m^3 for SMOS and SMAP respectively).

We characterize the amplitude of the SSM annual peaks by the maximum value of SSM anomaly between December and March (resp. May and November) in the dry (resp. wet) season. Table I reports the Pearson correlation coefficients between the amplitude of the 3 SSM datasets and the percentage of rice cover (obtained from land cover maps produced as explained in section II-B1) for the dry and wet seasons between 2016 and 2019. The last line presents the correlation coefficients for all years, cumulating both the spatial and temporal effects. Rice cover and SSM SMOS L3 and SMAP L3E show the same spatial pattern (as illustrated for the dry season of 2018 in figure 3a), resulting in spatial correlations close to 1 in Table I (0.81 and 0.77 on average for SMOS and SMAP L3, respectively). Correlations between rice cover and the SSM peak amplitude are weaker in the 2016 and 2019 dry seasons due to the low SSM peak amplitude caused by the low extent of rice planting in both exceptionally dry years. Correlations tend to be lower during the wet season because the SSM amplitude is due both to rainfall and irrigation. The spatial correlations with SSM SMAP L4 are much lower than with L3 SSM products.

To go further, we investigated the impact of rainfall during the wet season by removing the effect of rainfall on the SSM dynamics (using a simple correction of SSM based on a linear regression between SSM and rainfall). Interestingly, such a correction increases the correlation between the amplitude of SMOS SSM and the percentage of rice cover from 0.76 to 0.83 and from 0.65 to 0.77 for the wet season of 2018 and 2019, respectively.

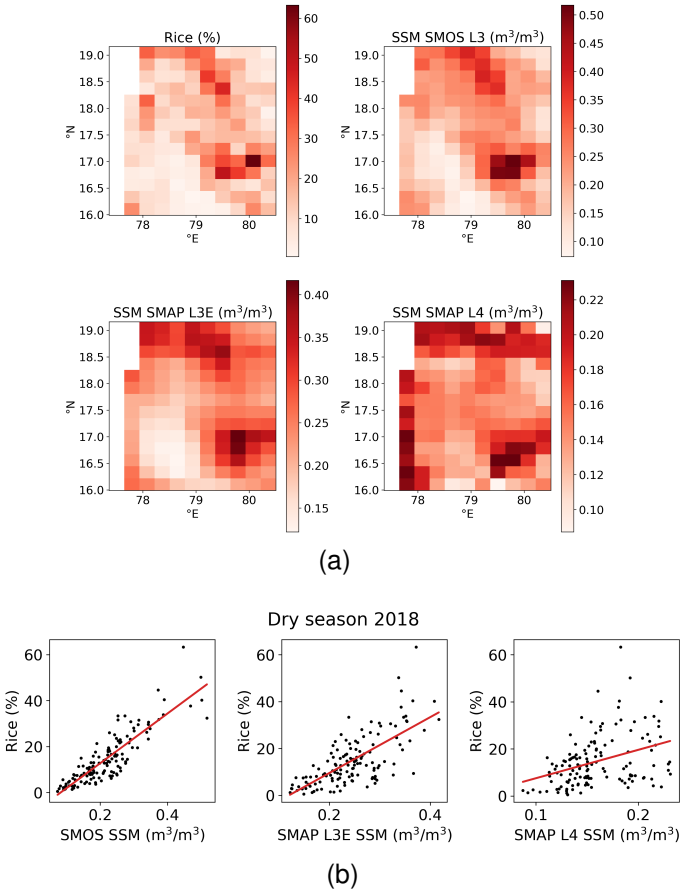

Fig. 3. (a) Maps of rice cover (%) and amplitude of the peak during the 2018 dry season for SMOS L3, SMAP L3E and SMAP L4 SSM (m^3/m^3) (obtained by subtracting the temporal average of SSM values between 2016 and 2019 pixel-wise). (b) Scatterplot of rice cover and the SSM products. The linear regression fit to the data points is indicated by the red line.

IV. CONCLUSION

SMOS and SMAP L-band data have been used for irrigation mapping and irrigation water quantification because of their sensitivity to soil moisture and open water. Prior to retrieving SSM from Tb observations, the SMOS and SMAP algorithms remove the contribution of saturated surfaces using maps at a typical 1 km resolution (e.g. ECOCLIMAP) of permanent surface water. However, permanent surface water is scarce in Telangana: hundreds of large dams and ∼45,000 small reservoirs fill with each monsoon and empty with domestic and agricultural water use. These strong dynamics are now available in high-resolution global surface water products [29] but are not yet reflected in the SSM restitution algorithms. Therefore, studies are needed to evaluate in real cases the impact of irrigated crops on the SMOS and SMAP SSM data.

This study demonstrates for the first time the potential of SMOS and SMAP L3 SSM data to quantify the fraction of flood-irrigated crops within a 25 km pixel in Telangana, a State in southern India. Areas with a large fraction of cultivated rice present a clear bimodal annual cycle with two peaks of SSM. One peak occurs during the wet season and is associated with the combined effect of rainfall and irrigation, while the other peak occurs during the dry season and is due to irrigation

alone. We identified a high correlation (R=0.81) between rice cover percentage and the amplitude of the SSM peak in the dry season, and a relatively lower correlation (R=0.68) in the wet season. The correlation is closer to 1 in the dry season than in the wet season because the spatial variability of rainfall disturbs the relationship between SMOS/SMAP SSM and irrigated areas in the wet season. Interestingly, if the effect of precipitation in the wet season is removed, the correlation reaches values (R=0.80) almost as high as those in the dry season. This approach could be used in combination with the knowledge of rice water needs and cultural practices to estimate the water used for irrigation.

ACKNOWLEDGMENTS

Field data for the production of land cover maps were surveyed with the help of the IFCGR (Indo-French Center for Groundwater Research), an Indo-French collaboration between the BRGM (Bureau des ressources géologiques et minières) and the NGRI (Indian National Geophysical Research Institute). Support from the Horizon 2020 ACCWA project (grant agreement n°823965) in the context of Marie Sklodowska-Curie research and innovation staff exchange (RISE) program is acknowledged.

REFERENCES

[1] J. A. Foley, N. Ramankutty, K. A. Brauman, E. S. Cassidy, J. S. Gerber, M. Johnston, N. D. Mueller, C. O'Connell, D. K. Ray, P. C. West, C. Balzer, E. M. Bennett, S. R. Carpenter, J. Hill, C. Monfreda, S. Polasky, J. Rockström, J. Sheehan, S. Siebert, D. Tilman, and D. P. M. Zaks, "Solutions for a cultivated planet," *Nature*, vol. 478, no. 7369, pp. 337–342, Oct. 2011.

[2] Y. Wada, D. Wisser, and M. F. P. Bierkens, "Global modeling of withdrawal, allocation and consumptive use of surface water and groundwater resources," *Earth System Dynamics*, vol. 5, no. 1, pp. 15–40, Jan. 2014.

[3] M. Rahman, L. Di, E. Yu, L. Lin, C. Zhang, and J. Tang, "Rapid Flood Progress Monitoring in Cropland with NASA SMAP," *Remote Sensing*, vol. 11, no. 2, p. 191, Jan. 2019.

[4] O. Calla, K. Gadri, R. Sharma, S. Agrahari, A. Kalla, and G. Rathore, "Microwave remote sensing application for monitoring of floods," *MAUSAM*, vol. 65, no. 2, pp. 141–152, Apr. 2014.

[5] J. Du, J. S. Kimball, J. Galantowicz, S.-B. Kim, S. K. Chan, R. Reichle, L. A. Jones, and J. D. Watts, "Assessing global surface water inundation dynamics using combined satellite information from SMAP, AMSR2 and Landsat," *Remote Sensing of Environment*, vol. 213, pp. 1–17, Aug. 2018.

[6] E. Fluet-Chouinard, B. Lehner, L.-M. Rebelo, F. Papa, and S. K. Hamilton, "Development of a global inundation map at high spatial resolution from topographic downscaling of coarse-scale remote sensing data," *Remote Sensing of Environment*, vol. 158, pp. 348–361, Mar. 2015.

[7] J. Du, J. S. Kimball, L. A. Jones, and J. D. Watts, "Implementation of satellite based fractional water cover indices in the pan-Arctic region using AMSR-E and MODIS," *Remote Sensing of Environment*, vol. 184, pp. 469–481, Oct. 2016.

[8] B. T. Gouweleeuw, A. I. J. M. van Dijk, J. P. Guerschman, P. Dyce, and M. Owe, "Space-based passive microwave soil moisture retrievals and the correction for a dynamic open water fraction," *Hydrology and Earth System Sciences*, vol. 16, no. 6, pp. 1635–1645, Jun. 2012.

[9] M. Parrens, A. Al Bitar, F. Frappart, F. Papa, S. Calmant, J.-F. Crétaux, J.-P. Wigneron, and Y. Kerr, "Mapping Dynamic Water Fraction under the Tropical Rain Forests of the Amazonian Basin from SMOS Brightness Temperatures," *Water*, vol. 9, no. 5, p. 350, May 2017.

[10] M. Parrens, A. A. Bitar, F. Frappart, R. Paiva, S. Wongchuig, F. Papa, D. Yamasaki, and Y. Kerr, "High resolution mapping of inundation area in the Amazon basin from a combination of L-band passive microwave, optical and radar datasets," *International Journal of Applied Earth Observation and Geoinformation*, vol. 81, pp. 58–71, Sep. 2019.

[11] P. M. Lawston, J. A. Santanello Jr, and S. V. Kumar, "Irrigation Signals Detected From SMAP Soil Moisture Retrievals," *Geophysical Research Letters*, vol. 44, no. 23, pp. 11,860–11,867, 2017.

[12] M. J. Escorihuela and P. Quintana-Seguí, "Comparison of remote sensing and simulated soil moisture datasets in Mediterranean landscapes," *Remote Sensing of Environment*, vol. 180, pp. 99–114, Jul. 2016.

[13] J. Dari, P. Quintana-Seguí, M. J. Escorihuela, V. Stefan, L. Brocca, and R. Morbidelli, "Detecting and mapping irrigated areas in a Mediterranean environment by using remote sensing soil moisture and a land surface model," *Journal of Hydrology*, vol. 596, p. 126129, May 2021.

[14] S. V. Kumar, C. D. Peters-Lidard, J. A. Santanello, R. H. Reichle, C. S. Draper, R. D. Koster, G. Nearing, and M. F. Jasinski, "Evaluating the utility of satellite soil moisture retrievals over irrigated areas and the ability of land data assimilation methods to correct for unmodeled processes," *Hydrology and Earth System Sciences*, vol. 19, no. 11, pp. 4463–4478, Nov. 2015.

[15] L. Brocca, A. Tarpanelli, P. Filippucci, W. Dorigo, F. Zaussinger, A. Gruber, and D. Fernández-Prieto, "How much water is used for irrigation? A new approach exploiting coarse resolution satellite soil moisture products," *International Journal of Applied Earth Observation and Geoinformation*, vol. 73, pp. 752–766, Dec. 2018.

[16] J. Dari, L. Brocca, P. Quintana-Seguí, M. J. Escorihuela, V. Stefan, and R. Morbidelli, "Exploiting High-Resolution Remote Sensing Soil Moisture to Estimate Irrigation Water Amounts over a Mediterranean Region," *Remote Sensing*, vol. 12, no. 16, p. 2593, Jan. 2020.

[17] P. Filippucci, A. Tarpanelli, C. Massari, A. Serafini, V. Strati, M. Alberi, K. G. C. Raptis, F. Mantovani, and L. Brocca, "Soil moisture as a potential variable for tracking and quantifying irrigation: A case study with proximal gamma-ray spectroscopy data," *Advances in Water Resources*, vol. 136, p. 103502, Feb. 2020.

[18] E. Jalilvand, M. Tajrishy, S. A. Ghazi Zadeh Hashemi, and L. Brocca, "Quantification of irrigation water using remote sensing of soil moisture in a semi-arid region," *Remote Sensing of Environment*, vol. 231, p. 111226, Sep. 2019.

[19] L. Brocca, L. Ciabatta, C. Massari, T. Moramarco, S. Hahn, S. Hasenauer, R. Kidd, W. Dorigo, W. Wagner, and V. Levizzani, "Soil as a natural rain gauge: Estimating global rainfall from satellite soil moisture data," *Journal of Geophysical Research: Atmospheres*, vol. 119, no. 9, pp. 5128–5141, 2014.

[20] J. Peng, A. Loew, O. Merlin, and N. E. C. Verhoest, "A review of spatial downscaling of satellite remotely sensed soil moisture," *Reviews of Geophysics*, vol. 55, no. 2, pp. 341–366, 2017.

[21] S. Ferrant, A. Selles, M. Le Page, P.-A. Herrault, C. Pelletier, A. Al-Bitar, S. Mermoz, S. Gascoin, A. Bouvet, M. Saqalli, B. Dewandel, Y. Caballero, S. Ahmed, J.-C. Maréchal, and Y. Kerr, "Detection of Irrigated Crops from Sentinel-1 and Sentinel-2 Data to Estimate Seasonal Groundwater Use in South India," *Remote Sensing*, vol. 9, no. 11, p. 1119, Nov. 2017.

[22] J. Inglada, A. Vincent, M. Arias, B. Tardy, D. Morin, and I. Rodes, "Operational High Resolution Land Cover Map Production at the Country Scale Using Satellite Image Time Series," *Remote Sensing*, vol. 9, no. 1, p. 95, Jan. 2017.

[23] G. Pingle, "Irrigation in Telangana: The Rise and Fall of Tanks," *Economic & Political Weekly*, p. 9, 2011.

[24] U. Surendran, P. Raja, M. Jayakumar, and S. R. Subramoniam, "Use of efficient water saving techniques for production of rice in india under climate change scenario: A critical review," *Journal of Cleaner Production*, vol. 309, p. 127272, 2021. [Online]. Available: https://www.sciencedirect.com/science/article/pii/S0959652621014918

[25] O. Hagolle, M. Huc, C. Desjardins, S. Auer, and R. Richter, "MAJA Algorithm Theoretical Basis Document," Dec. 2017.

[26] A. Al Bitar, A. Mialon, Y. H. Kerr, F. Cabot, P. Richaume, E. Jacquette, A. Quesney, A. Mahmoodi, S. Tarot, M. Parrens, A. Al-Yaari, T. Pellarin, N. Rodriguez-Fernandez, and J.-P. Wigneron, "The global SMOS Level 3 daily soil moisture and brightness temperature maps," *Earth System Science Data*, vol. 9, no. 1, pp. 293–315, Jun. 2017.

[27] M. J. Brodzik, B. Billingsley, T. Haran, B. Raup, and M. H. Savoie, "EASE-Grid 2.0: Incremental but Significant Improvements for Earth-Gridded Data Sets," *ISPRS International Journal of Geo-Information*, vol. 1, no. 1, pp. 32–45, Jun. 2012.

[28] R. Reichle, R. Koster, G. D. Lannoy, W. Crow, and J. Kimball, "Level 4 Surface and Root Zone Soil Moisture (L4_SM) Data Product," Dec. 2014.

[29] J.-F. Pekel, A. Cottam, N. Gorelick, and A. S. Belward, "High-resolution mapping of global surface water and its long-term changes," *Nature*, vol. 540, no. 7633, pp. 418–422, Dec. 2016.